American Mineralogist, Volume 107, pages 421–431, 2022

Measurements of the Lamb-Mössbauer factor at simultaneous high-pressure-temperature conditions and estimates of the equilibrium isotopic fractionation of iron

Dongzhou Zhang[1,4,*], Jennifer M. Jackson[2], Wolfgang Sturhahn[2], Jiyong Zhao[3], E. Ercan Alp[3], and Michael Y. Hu[3]

[1]Hawaii Institute of Geophysics and Planetology, University of Hawaii at Manoa, Honolulu, Hawaii 96822, U.S.A.
[2]Seismological Laboratory, California Institute of Technology, Pasadena, California 91125, U.S.A.
[3]Advanced Photon Source, Argonne National Laboratory, Argonne, Illinois 60439, U.S.A.
[4]GSECARS, University of Chicago, Argonne, Illinois 60439, U.S.A.

Abstract

Isotopic fractionation has been linked to the lattice vibrations of materials through their phonon spectra. The Lamb-Mössbauer factor (f_{LM}) has the potential to provide information about the lattice vibrations in materials. We constrain the temperature evolution of the f_{LM} of γ- and ε-Fe at in situ high-*P*-*T* conditions between 1650 K and the melting point. We find that the vibrations of γ- and ε-Fe can be described using a quasiharmonic model with a pressure- and temperature-dependent Debye temperature computed from the measured f_{LM}. From the Debye temperature, we derive the equilibrium isotopic fractionation β-factor of iron. Our results show that the quasiharmonic behavior of metallic iron would lower the value of $\ln\beta_{Fe}^{57/54}$ by 0.1‰ at 1600–2800 K and 50 GPa when compared to the extrapolation of room temperature nuclear resonant inelastic X-ray scattering data. Our study suggests that anharmonicity may be more prevalent in Fe metal than in lower mantle minerals at 2800 K and 50 GPa, a relevant condition for the core formation, and the silicate mantle may be isotopically heavy in iron.

Keywords: Iron isotope fractionation, high pressure-temperature, Mossbauer spectroscopy, anharmonicity

Introduction

Studies of the collective atomic oscillations in crystalline materials, or quantized lattice vibrations (phonons), are important for understanding and predicting the behavior of earth materials (e.g., Reynard et al. 2015). For example, acoustic phonons at the long-wavelength limit are intricately related to the elastic properties of minerals and affect seismic wave propagation within the Earth (Lin et al. 2005; Sturhahn and Jackson 2007; Zhang et al. 2013; Murphy et al. 2013; Chen et al. 2014; Wicks et al. 2017). Measurements of the phonon density of states as a function of pressure provide constraints on important thermodynamic parameters, including the vibrational free energy, entropy, and kinetic energy (e.g., Murphy et al. 2013; Morrison et al. 2019). Understanding phonon behavior in minerals provides estimates on the thermal budget of the Earth, as heat is mainly stored and transported via vibrational excitations (Chai et al. 1996; Jeanloz and Morris 1986; Jeanloz and Richter 1979; Kieffer 1979a, 1979b, 1979c, 1980, 1982). Studies of lattice vibrations have led to a better understanding of phase transitions (e.g., Wentzcovitch et al. 2010; Yu et al. 2008, 2010), including melting (Shen and Heinz 1998; Alfè et al. 1999, 2002, 2004; Vočadlo and Alfe 2002). Geochemical studies have demonstrated that mantle derived rocks are ~0.1‰ heavier in δ^{57}Fe than chondrite (Poitrasson et al. 2004; Sossi et al. 2016), and measurements of lattice vibrational properties of minerals and glasses are used to constrain whether the core formation would leave such isotopic signature to mantle rocks (Polyakov 2009; Shahar et al. 2016; Liu et al. 2017).

Lattice vibrations are determined by the interatomic potential (e.g., Reynard et al. 2015; Fultz 2010). In the harmonic approximation, the interatomic potential is quadratic in the vicinity of the atomic equilibrium positions (e.g., Dunitz et al. 1988; Trueblood et al. 1996; Sturhahn and Jackson 2007; Reynard et al. 2015). The harmonic approximation assumes that phonon spectra do not change with temperature. Although the harmonic approximation is used to explain selected physical properties of some solids under particular conditions (mostly at low temperatures), this model often fails to explain or predict material behavior under a wide range of conditions (Polyakov 1998; Fultz 2010; Wu 2010; Mauger et al. 2014). Several components contribute to the deviation from harmonicity in solids and are described by different physical models. Often-used models to describe nonharmonic lattice vibrations are quasiharmonic approximations, which allow temperature- and/or pressure-induced volume changes while assuming harmonic, non-interacting phonons (Polyakov 1998; Fultz 2010; Wu 2010; Mauger et al. 2014; Allen 2020).

Under some conditions, particularly at high temperatures, higher-order terms of the interatomic potential are required to describe the atomic displacements, and the anharmonicity is dominated by phonon-phonon interactions. These effects are sometimes named "intrinsic anharmonicity" (Polyakov 1998; Sturhahn and Jackson 2007; Fultz 2010; Reynard et al. 2015; Bansal et al. 2016; Allen 2020). In addition to phonon-phonon interactions, electron-phonon and magnon-phonon interactions might be included in the description of "intrinsic anharmonicity" (Fultz 2010; Mauger et al. 2014; Bansal et al. 2016). Anharmonicity is the origin of several important physical properties in solids, such as thermal expansion and lattice thermal conductivity (e.g.,

* E-mail: dzhang@hawaii.edu. Orcid 0000-0002-6679-892X

Reynard et al. 2015) and various other experimentally observable effects (Tse et al. 2005; Brown 1969; Chumakov et al. 1996; Mauger et al. 2014; Kim et al. 2018).

Here we assume weak anharmonicity, which permits us to use a quasiharmonic model for the lattice vibrations. A description of the lattice vibrations via the phonon density of states (DOS) can be determined experimentally, e.g., by inelastic X-ray/neutron scattering or nuclear resonant inelastic X-ray scattering. However, in many cases, a contraction of the DOS, such as specific heat or mean-square atomic displacement, is experimentally accessible. Our data provide us with the Lamb-Mössbauer factor of hot compressed iron, which for our quasiharmonic model is related to the mean-square displacement of the iron atoms:

$$\langle u^2 \rangle = -\frac{1}{k_0^2} \ln f_{LM} \quad (1)$$

where k_0 = 7.306 Å^{-1} is the wavenumber of the 14.4125 keV X-rays that corresponds to the nuclear resonant energy level of iron (Sturhahn 2004). The atomic mean square displacement $\langle u^2 \rangle$ is the quantum-mechanical time-average of the square of atomic displacement with respect to its equilibrium position (Singwi and Sjölander 1960; Sturhahn and Chumakov 1999), and the close relationship between the atomic mean square displacement $\langle u^2 \rangle$ and the DOS has been described earlier (Singwi and Sjölander 1960; Dunitz et al. 1988; Trueblood et al. 1996; Sturhahn and Chumakov 1999). A harmonic model gives a linear temperature behavior for sufficiently high temperatures $\lim_{T\to\infty} \langle u^2 \rangle \propto T$. Deviations from this asymptotic linearity are interpreted as resulting from anharmonicity.

Using Mössbauer spectroscopy data, the equilibrium isotopic fractionation β-factor was first estimated from the second-order Doppler shift (Polyakov 1997; Polyakov and Mineev 2000). More recently, using nuclear resonant inelastic X-ray scattering (NRIXS), the general moments (GM) method has been developed to estimate the iron isotopic fractionation between minerals from their lattice vibrational properties (Polyakov et al. 2007; Polyakov 2009; Dauphas et al. 2012, 2018). In the GM method, the equilibrium isotopic fractionation β-factor of each mineral is calculated either from the moments of the iron nuclear resonant inelastic X-ray scattering spectrum (Polyakov et al. 2007; Polyakov 2009), or from the mean force constants (stiffness) derived from the iron partial phonon DOS (Dauphas et al. 2012; Shahar et al. 2016; Liu et al. 2017), or both (Murphy et al. 2013; Dauphas et al. 2018). A few recent studies have used this GM approach to estimate the iron isotopic fingerprints on the bulk silicate earth during the core-formation process (Shahar et al. 2016; Liu et al. 2017). Most of the studies using the GM approach extrapolate room temperature NRIXS results to high temperatures without considering deviations from harmonicity. Studies have suggested that the deviation from harmonicity of lattice vibrations lowers the β-factor and that the quasiharmonic correction has a more pronounced effect than the intrinsic anharmonic component (Polyakov 1998, 2009).

Mössbauer spectroscopy is a suitable method to measure the Lamb-Mössbauer factor, which is the probability of recoilless scattering of nuclear resonant X-rays, under various experimental conditions (Sturhahn 2004; Sturhahn and Jackson 2007). One can calculate the temperature dependence of $\langle u^2 \rangle$ from the temperature dependence of f_{LM} using Equation 1. f_{LM} varies with material composition, lattice or local atomic structure, and experimental conditions, such as temperature or pressure (Bergmann et al. 1994; Chumakov et al. 1996; Shen et al. 2004; Lin et al. 2005; Jackson et al. 2013; Zhang et al. 2016; Morrison et al. 2019). However, the relationship between Lamb-Mössbauer factor and isotopic fractionation has not been established and is presented here as an important innovation for the study of isotopic fractionation in solids at high temperatures.

The physical and chemical properties of iron at elevated pressure-temperature conditions are important to understand the internal structure and evolution of the Earth. In addition to the liquid state, iron is known to have three major allotropes at elevated pressure-temperature conditions: the body-centered cubic (α) phase, the face-centered cubic (γ) phase, and the hexagonal close-packing (ε) phase. The f_{LM} of α-Fe has been measured at various temperatures from 4 to ~1300 K using conventional Mössbauer spectroscopy (Kolk et al. 1986; Kovats and Walker 1969), NRIXS (Chumakov and Sturhahn 1999; Mauger et al. 2014), and synchrotron Mössbauer spectroscopy (SMS) [Bergmann et al. (1994), room pressure only]. The f_{LM} of ε-Fe has been studied with NRIXS up to 171 GPa at 300 K (Murphy et al. 2013; Morrison et al. 2019) and up to 73 GPa at temperatures below 1700 K (Shen et al. 2004; Lin et al. 2005). Limited measurements on the f_{LM} of γ-Fe have been carried out at room pressure (Kovats and Walker 1969; Mauger et al. 2014). The f_{LM} of γ-Fe has never been systematically studied at high pressures. Measuring the f_{LM} of iron at temperatures above 1700 K is challenging using conventional Mössbauer spectroscopy and NRIXS, because the recoil-free fraction decreases with temperature, and it is very difficult to maintain a stable uniform sample temperature over the long data collection times required to obtain a statistically meaningful result (several hours to days).

We have measured the Lamb-Mössbauer factor of iron at elevated pressures and temperatures using synchrotron Mössbauer spectroscopy. Our method combines the laser-heated diamond-anvil cell (DAC), the recently developed fast temperature readout spectrometer (FasTeR) for accurate and precise temperature determinations, and the SMS technique to monitor the atomic dynamics of the iron nuclei (Singwi and Sjölander 1960; Boyle et al. 1961; Jackson et al. 2013; Zhang et al. 2015, 2016), while constraining the evolution of the effective thickness of the sample. This approach is capable of determining the f_{LM}, and thus iron's atomic mean square displacement, up to its melting point at elevated pressures. From the f_{LM} data, we present a quasiharmonic correction to iron's isotope fractionation β-factor at elevated pressure-temperature conditions, and discuss its potential geochemical implications to Earth's core formation process.

Experiments to determine the Lamb-Mössbauer factor at high-*P*-*T* conditions

In our experiment, a symmetric DAC is used to provide the high-pressure environment. Two Type-I diamonds with 300 μm culet are mounted and aligned to form the anvils. A Re gasket is pre-indented to ~45 μm thick, and a 115 μm

diameter hole is drilled in the center of the pre-indention using a laser drilling system. A 95% isotopically enriched ^{57}Fe foil with 3 μm thickness is cut into a 70 × 70 μm^2 square section and cleaned. Note the ^{57}Fe samples used here are from the same larger foil used in previous studies (Jackson et al. 2013; Murphy et al. 2013; Zhang et al. 2016). Dehydrated KCl is pressed into transparent flakes and loaded together with the foils in a sandwich configuration into the Re gasket. The KCl serves as both a pressure-transmitting medium and thermal insulator. The DAC is heated in a vacuum furnace overnight before closing to remove the moisture.

The experiments are carried out at beamline 3-ID-B at the Advanced Photon Source, and the experimental setup is illustrated in Zhang et al. (2015). The storage ring is operated in low-emittance top-up mode with 24 bunches that are separated by 153 ns. The energy (14.4125 keV) and resolution (1 meV) of the X-rays are determined by a silicon high-resolution monochromator (Toellner 2000) and a focus area of ~10 × 14 μm (full-width at half maximum) is achieved by a Kirkpatrick-Baez mirror system. In situ angular-dispersive X-ray diffraction (XRD) patterns are collected at beamline 3-ID-B using 14.4125 keV X-ray to constrain the crystal symmetry and unit-cell parameters, which are used to compute the pressure using the equation of state of iron (see below). A high-resolution MAR image plate, located ~0.3 m downstream from the DAC, is used to collect the XRD patterns. Each XRD pattern is collected for ~30 min. A CeO_2 standard sample is used to calibrate the sample to image plate distance and correct the tilt of the image plate. The diffraction images are integrated into angular resolved intensity files using the DIOPTAS software (Prescher and Prakapenka 2015). In our experiments, ε-Fe is observed in both runs at ambient temperature. The 300 K equations of state of ε-Fe from Fei et al. (2016) are used to calculate the pressure at room temperature. All the samples are laser-annealed at 1500 K for ~30 min before XRD measurements are collected so as to release the residual deviatoric stress and reduce the pressure gradient on the sample. After the heating run, we collect another XRD pattern at 300 K to constrain any pressure drift. We report the pressure computed using the XRD measurements at the sample location where the heating experiment is applied. We estimate the thermal contribution to the pressure using the empirical equation from our previous study utilizing a similar sample configuration: $\Delta P = a(T - 300\text{K}) + c(T^2 - 90\,000\text{K}^2)$, where $a = 4.6 \times 10^{-3}$ GPa/K, $c = 2 \times 10^{-6}$ GPa^2/K^2, and an additional 2 GPa is added to the pressure uncertainty in Table 1 due to the scatter in the thermal pressure contribution (Zhang et al. 2016).

The experimental setup of the SMS measurement is similar to that of the XRD, and an avalanche photodiode is placed ~0.5 m downstream from the sample (Zhang et al. 2015). As stated above, the samples in each DAC are laser-annealed prior to the following experimental procedure. An SMS spectrum is first collected at room temperature (300 K) as a reference on the sample position where the high-temperature measurement will be carried out. The room-temperature SMS spectrum provides two pieces of information: the time interval used to collect the time-resolved SMS signal (also known as the timing window of the experiment, see Sturhahn 2001) and the effective thickness of the sample before the series of high-temperature measurements. The profile of the time-resolved delayed counts, S, is a function depending on the level splitting of the resonant nuclei and the effective thickness of the sample, η. The effective thickness is a dimension-less number given as the product of the numerical density of the ^{57}Fe nuclei, ρ, the physical thickness of the sample, d, the nuclear resonant cross section, $\sigma = 2.56 \times 10^{-22}$m^2, and the f_{LM}:

$$\eta = \rho d \sigma f_{LM}. \quad (2)$$

For γ- and ε-Fe, it is known that the nuclear levels of ^{57}Fe are unsplit (Macedo and Keune 1988). Therefore, S reduces to:

$$S(t,\eta) = \eta^2 e^{-t/\tau} \frac{J_1^2(\sqrt{\eta t/\tau})}{\eta t/\tau} \quad (3)$$

where t is the time delay from the exciting X-ray bunch, J_1 is the first-order Bessel function of the first kind, and τ is the life time of the excited nuclear state (141 ns for ^{57}Fe) (Sturhahn 2000; Jackson et al. 2013). By fitting the room-temperature SMS spectrum with Equation 3, the effective thickness distribution at 300 K is obtained (Fig. 1). Since the f_{LM} of ε-Fe has been measured as a function of pressure (Murphy et al. 2013), one can calculate the physical thickness distribution from the effective thickness distribution.

The next step is to determine the effective thickness as a function of temperature by monitoring the temperature evolution of the integrated SMS signal (delayed counts). We proceed to heat both sides of the sample to 1650 K and balance the temperatures read from a charge-coupled device (CCD) detector so that the sample is heated uniformly (Jackson et al. 2013; Zhang et al. 2015, 2016). The temperature difference of the upstream and downstream sides of the sample is found to be smaller than 10 K. We collect a high-temperature SMS spectrum and determine the effective thickness under these conditions (Fig. 1). After the high-temperature SMS measurement, we proceed with a computer-acquisition program to ramp up the laser power until the sample melts while simultaneously monitoring the delayed counts, the temperature of the sample, and the readings of ion chambers (Jackson et al. 2013; Zhang et al. 2016). Each temperature is held for 3 s, which is enough for the sample to reach thermal relaxation and equilibration (Anzellini et al. 2013). The temperature of the sample is monitored by the FasTeR spectrometer and CCD detector (Zhang et al. 2015), and the reported temperature error incorporates the fluctuation of the ~300 FasTeR readings within the 3 s data collection time, and the estimated 10 K temperature difference between the upstream and downstream sides of the sample (Zhang et al. 2016). The melting point is determined from fits to the data set of normalized SMS delayed counts as a function of temperature using the MINUTI software package (Sturhahn 2020; Zhang et al. 2015). Due to the finite timing window, the delayed counts are not directly proportional to the effective thickness. The delayed counts are first normalized with the readings from ion chambers, which is proportional to the incident X-ray photon flux. Then, the normalized delayed counts are converted to effective thickness using the following equation (Fig. 2):

$$I(\eta) = A e^{-\mu d} \sum_{n=0}^{\infty} \int_{t_1+nt_B}^{t_2+nt_B} S(t',\eta) dt' \quad (4)$$

where t_1 and t_2 are the beginning and end of the time window accessible from the SMS spectrum, t_B is the time interval between X-ray pulses given by the synchrotron operation mode (in our case t_B = 153 ns), A is a scaling factor that depends on experimental conditions such as spectral X-ray flux incident on the sample, d is the physical thickness of the sample, μ is the electronic absorption coefficient of the sample material, S is the profile of time-resolved delayed counts described in Equation 3, and η is the effective thickness of the sample (Jackson et al. 2013). In the data fitting, the starting effective thickness is constrained from the 1650 K SMS spectrum, and the effective thickness at the melting point is fixed as 0 (Zhang et al. 2016).

After determining the effective thickness of the sample at different temperatures, the f_{LM} is then calculated from Equation 2. To calculate f_{LM}, one needs to estimate the variation of the numerical density of resonant nuclei over the experimental time scale. We estimate the upper limit of the variation in the numerical density of resonant nuclei using the data collected at the lowest and highest temperatures. At 1656 K and 54 GPa (ε-Fe), the calculated numerical density of resonant nuclei is 0.1779 mol/cm^3 (Fei et al. 2016). At 2842 K and 57 GPa (γ-Fe), the calculated numerical density of resonant nuclei is 0.1785 mol/cm^3 (Komabayashi and Fei 2010). The estimated upper limit of the variations in numerical density during the experiment is 0.35%, much smaller than the experimental error. To simplify the calculation, we assume that the numerical density of resonant nuclei does not change during the experiment. By assuming that the sample chamber's thickness does not change during the experiment, as verified by X-ray absorption scans across the chamber before and after each heating cycle, the change of the physical thickness (Δd) is monitored using the ion chambers upstream and downstream from the sample:

TABLE 1. Lamb-Mössbauer factor and β-factor of iron at various temperatures and pressures determined in this study

Run 1				Run 2			
T (K)	P (GPa)	f_{LM}	ln$\beta_{57/54}$ (‰)	T (K)	P (GPa)	f_{LM}	ln$\beta_{57/54}$ (‰)
1656(61)	54(3)	0.41(9)	0.38(8)	1675(53)	51(4)	0.41(6)	0.37(6)
1957(78)	55(3)	0.38(8)	0.29(6)	1740(60)	51(4)	0.43(7)	0.38(7)
2107(42)	56(3)	0.30(8)	0.22(5)	1988(88)	53(4)	0.28(3)	0.22(2)
2330(51)	57(3)	0.24(3)	0.17(1)	2173(35)	54(4)	0.183(7)	0.151(3)
2459(43)	58(3)	0.24(5)	0.16(2)	2266(64)	54(4)	0.180(6)	0.143(3)
2552(44)	59(3)	0.11(1)	0.101(4)	2431(34)	55(4)	0.20(2)	0.14(1)
2574(55)	59(3)	0.092(8)	0.091(3)	2377(32)	55(4)	0.16(2)	0.129(7)
2655(80)	59(3)	0.11(1)	0.094(4)	2438(41)	55(4)	0.14(1)	0.117(5)
2695(54)	59(3)	0.082(7)	0.083(3)	2425(22)	55(4)	0.108(9)	0.103(4)
2640(93)	59(3)	0.079(7)	0.083(3)	2474(43)	55(4)	0.16(1)	0.123(6)
2642(89)	59(3)	0.14(1)	0.108(6)	2540(45)	56(4)	0.17(2)	0.122(6)
2813(53)	60(3)	0.0(0)	NA	2635(48)	56(4)	0.12(1)	0.102(4)
				2578(52)	56(4)	0.065(6)	0.079(3)
				2586(33)	56(4)	0.13(1)	0.105(4)
				2677(36)	56(4)	0.061(6)	0.074(2)
				2717(20)	57(4)	0.068(6)	0.076(3)
				2764(31)	57(4)	0.019(4)	0.051(2)
				2842(19)	57(4)	0.0(0)	NA

Notes: Numbers in parentheses indicate the error bar rounded to the last significant digit. At the melting point the β-factor is not available due to the divergence when calculating ⟨u^2⟩ using Equation 1.

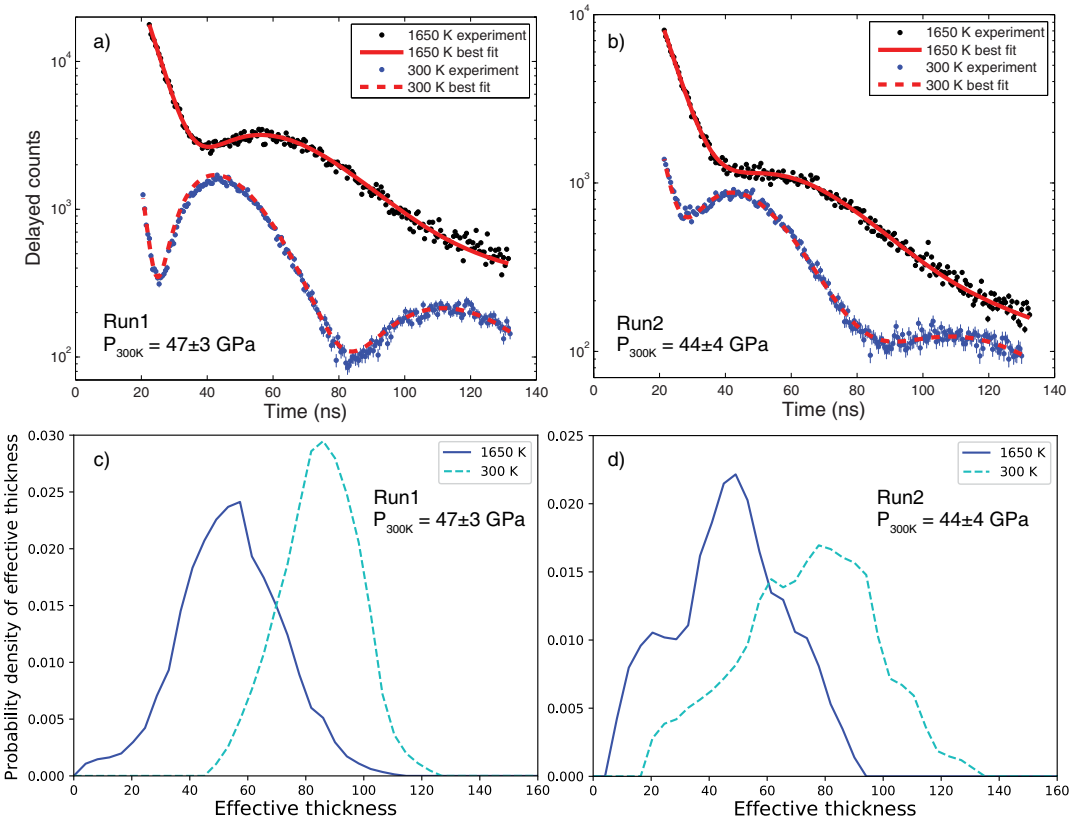

Figure 1. SMS spectra and fitted effective thickness distributions of iron at 300 and 1650 K at elevated pressures. Top panels: Synchrotron Mössbauer delayed counts (S) as a function of time (Eq. 3), from which the effective thickness (η) is fitted. Bottom panels: Best-fit probability density of effective thicknesses (η) at different temperatures. The area integration under each curve is 1. The η at higher temperature is expected to be smaller than η at lower temperatures, because f_{LM} decreases with temperature. The physical thickness of the sample changed <6% during the experiment, and the change in η was dominated by the decrease of f_{LM} with temperature. (Color online.)

$$\Delta d = \frac{A - A_0}{1/\mu_{KCl} - 1/\mu_{Fe}} \quad (5)$$

where μ_{KCl} and μ_{Fe} are the attenuation lengths of KCl and Fe at 14.4125 keV (Henke et al. 1993), A is the normalized X-ray absorption constrained from the ion chambers before and after the sample at each temperature, and A_0 is the normalized X-ray absorption before heating. The f_{LM} at pressures ranging from around 50 to 60 GPa and a range of temperatures up to melting are listed in Table 1. We compare our results with previous NRIXS measurements on Fe (Shen et al. 2004; Lin et al. 2005; Mauger et al. 2014) at high pressures and temperatures (Fig. 3). We notice that the f_{LM} of γ- and ε-Fe have the following features: within the experimental error, the temperature dependence of the f_{LM} of γ-Fe and ε-Fe show a continuous linear trend up to melting, and the effect of temperature on the f_{LM} is more significant than the effect of pressure. Using these features, we build the following model (hereinafter referred to as the Lamb-Mössbauer factor with temperature or FLMT model) to calculate the f_{LM} of γ- and ε-Fe at elevated P-T conditions. We assume that the f_{LM} of iron is a linear function of temperature between 300 K and the melting point at the stability fields of γ- and ε-Fe. At the melting point, the f_{LM} of iron is fixed at zero (Jackson et al. 2013). So, we have:

$$f_{LM}(T) = \frac{T_{melt} - T}{T_{melt} - 300} f_{LM,300K} \quad (6)$$

In Equation 6, T_{melt} is the melting temperature of iron at the experimental pressure (Zhang et al. 2016). The f_{LM} of ε-Fe at 300 K is fitted as a function of pressure using an empirical equation (Murphy et al. 2013): $f_{LM,300\,K}(P) = C - Ae^{-BP}$, where $A = 0.115(3)$, $B = 0.012(1)$ GPa^{-1}, and $C = 0.936(4)$. As is shown in Equation 6, the FLMT model is not a linear fit to the f_{LM} data determined at different experimental temperatures.

From Quasiharmonic Debye Model to the Equilibrium Isotopic Fractionation Factor

Under the harmonic approximation, a solid with N atoms has 3N-6 independent phonons. The equations for the lattice vibrations can be solved exactly, and the f_{LM} can be calculated for the thermalized ensemble (Sturhahn and Jackson 2007; Murphy et al. 2013):

$$f_{LM} = \exp\left[-\int \frac{E_R}{E} \coth\left(\frac{E}{2k_B T}\right) g(E) dE\right] \quad (7)$$

where E_R is the recoil energy for the resonant nuclei (1.956 meV for ^{57}Fe, Sturhahn and Jackson 2007), E is the phonon energy, and $g(E)$ is the partial (or projected) phonon DOS. The quantity $g(E)$ is usually determined experimentally from an NRIXS spectrum (Sturhahn 2004). However, with only the f_{LM} available, it is not possible to determine the exact formulation of $g(E)$. When the exact formulation of $g(E)$ is not known, one needs to prescribe a model for $g(E)$. We assume weak anharmonicity,

which permits us to use a quasiharmonic model to describe the phonon behavior of iron. In the Debye model, $g(E)$ has the following form (Debye 1913; Singwi and Sjölander 1960; Leu and Sage 2016):

$$g(E)=\begin{cases}\dfrac{3E^2}{(\mathrm{k_B}\theta_D)^3} & (E\le \mathrm{k_B}\theta_D)\\ 0 & (E>\mathrm{k_B}\theta_D)\end{cases} \quad (8)$$

The parameter θ_D is the material-specific Debye temperature (Singwi and Sjölander 1960; Shen et al. 2004; Leu and Sage 2016). θ_D varies with unit-cell volume and is implicitly influenced by temperature through thermal expansion in the quasiharmonic Debye model (Baroni et al. 2010; Blanco et al. 2004). By combining Equations 1, 7, and 8, one can determine θ_D from $\langle u^2\rangle$ with the following relationship based on the Debye model (Singwi and Sjölander 1960; Shen et al. 2004):

$$-\frac{1}{k_0^2}\ln f_{LM}=\langle u^2\rangle=\frac{6E_R}{k_0^2\mathrm{k_B}\theta_D}\left[\frac{1}{4}+\left(\frac{T}{\theta_D}\right)^2\int_0^{\frac{\theta_D}{T}}\frac{x}{e^x-1}dx\right] \quad (9)$$

As discussed in the introduction, the harmonic approximation does not have a volumetric dependence of the lattice vibrational frequencies and thus has shortcomings such as zero thermal expansion, zero Grüneisen parameter, and infinite lattice thermal conductivity (Erba 2014; Blanco et al. 2004; Baroni et al. 2010). To overcome the drawbacks of the harmonic approximation, the quasiharmonic approximation is often used to describe the behavior of real solids (Sturhahn and Jackson 2007; Blanco et al. 2004; Mauger et al. 2014). The quasiharmonic approximation assumes the existence of phonons (hence the use of Eq. 7 is justified) but does not consider phonon-phonon interactions and introduces an explicit dependence of vibration phonon frequencies on volume (Erba 2014; Blanco et al. 2004; Mauger et al. 2014; Baroni et al. 2010; Wu 2010; Sturhahn and Jackson 2007). The quasiharmonic approximation holds for many solids, while it fails for liquids or fast atomic diffusion where the collective atomic motions are different from phonons (Sturhahn and Jackson 2007). In the scope of this paper, the quasiharmonic Debye model is used.

The equilibrium isotopic fractionation β-factor is defined as the equilibrium isotopic fractionation factor between a mineral phase that contains the element of interest (X) and the monatomic ideal gaseous phase of element X (Richet et al. 1977; Schauble 2011; Huang et al. 2013; Eldridge et al. 2016). β-factor can be expanded as a function of the even powers of the inverse temperature ($1/T$), and the coefficients of each term

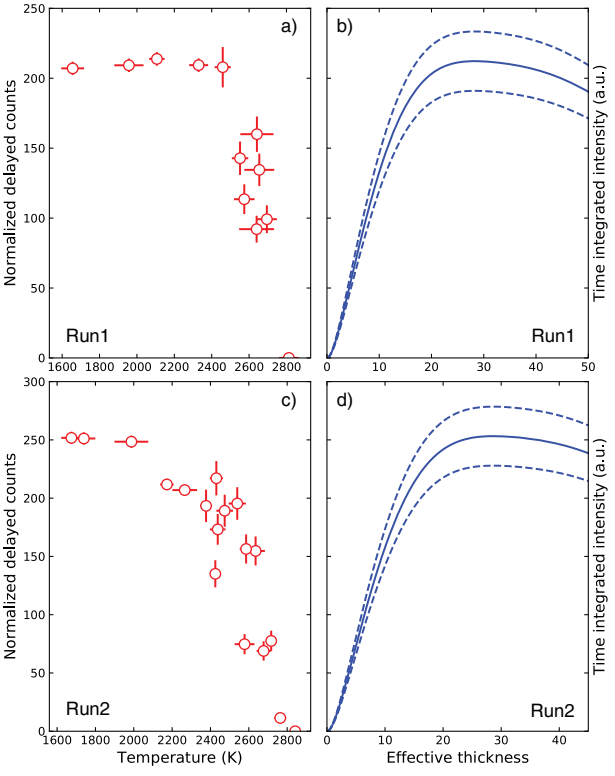

Figure 2. Determination of the effective thicknesses at different temperatures using SMS delayed counts. The evolution of pressure with temperature is noted in Table 1. The pressures at 300 K are 47 ± 3 GPa for Run 1 and 44 ± 4 GPa for Run 2. The theoretical curves (right panels) are calculated using the effective thickness determined by the 1650 K SMS spectrum (Fig. 1) and Equation 4, and then scaled with the maximum value of the measured SMS delayed counts (left panels). The effective thickness for each temperature is determined by projecting the measured SMS delayed counts to the corresponding theoretical curves. The maximum value of the measured normalized delayed counts are different between runs, because of the temporal drift in incident resonant X-ray flux and the variations in sample thickness. Dashed curves in **b** and **d** = error range of the theoretical curve calculated from Equation 4. (Color online.)

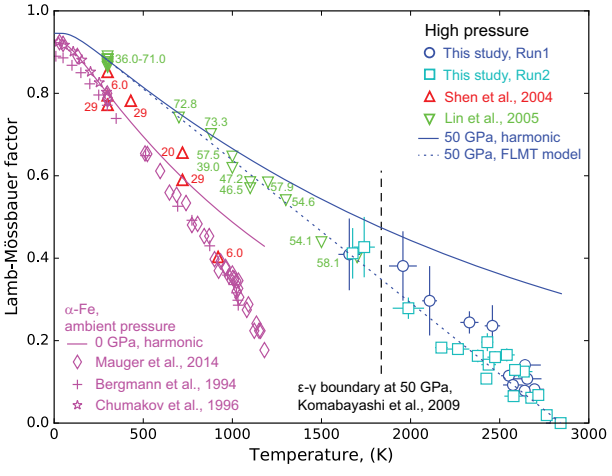

Figure 3. f_{LM} of iron at different pressures and temperatures. Magenta diamonds, crosses and stars = f_{LM} of α-Fe measured at room pressure by Mauger et al. (2014), Bergmann et al. (1994), and Chumakov et al. (1996), respectively. Magenta solid curve = f_{LM} calculated from harmonic model at 0 GPa. Red up triangles and green down triangles = f_{LM} of γ- and ε-Fe measured at high pressures by Shen et al. (2004) and Lin et al. (2005), respectively. Number next to each triangle indicates its pressure at 300 K. Blue circles and cyan squares = f_{LM} determined by this study. Blue solid curve = f_{LM} calculated from the harmonic model at 50 GPa. Blue dotted line = f_{LM} calculated from the FLMT model. Black dashed line shows the γ-ε phase boundary of Fe at 50 GPa (Komabayashi et al. 2009). (Color online.)

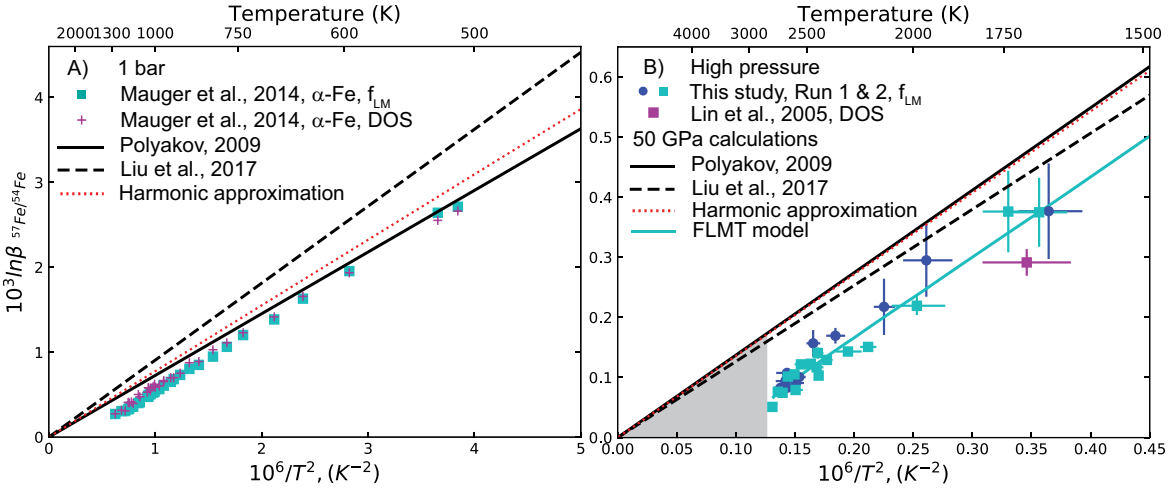

Figure 4. Equilibrium fractionation factor between ^{57}Fe and ^{54}Fe at different pressures and temperatures. (**a**) Data at 1 bar. Cyan squares: Mauger et al. (2014), calculated from the f_{LM} data using Equations 1 and 2. The f_{LM} in Mauger et al. (2014) is calculated using the PHOENIX software package. Magenta crosses = Mauger et al. (2014), calculated from the phonon DOS and the GM approach (Polyakov 2009; Dauphas et al. 2018). Black solid line = Polyakov (2009). Black dashed line = Liu et al. (2017), recalculated using equation $10^3\ln\beta_{57/54} = 1.47 \times 10^3\ln\beta_{56/54}$ (Young et al. 2002). Red solid line = β-factor calculated from harmonic approximation using Equations 1 and 2. Red dotted line = β-factor calculated from harmonic approximation shifted down by 0.1‰ as a visual reference. (**b**) Data at 51–60 GPa. Blue circles and cyan squares = iron β-factors determined by this study (Table 1). Magenta square = Lin et al. (2005), calculated from the phonon DOS and the general moments approach. Black solid line = 50 GPa data from Polyakov (2009). Black dashed line = 50 GPa data, recalculated from Liu et al. (2017). Red solid line = β-factor calculated from the harmonic approximation at 50 GPa. Red dotted line = β-factor calculated from harmonic approximation shifted down by 0.1‰ as a visual reference. Cyan line = β-factor calculated from the 50 GPa FLMT model. Shaded region = possible range for lnβ of Fe at temperatures above the melting point. (Color online.)

are determined by the Debye temperature θ_D (Polyakov and Mineev 2000; Polyakov et al. 2005). If one expands lnβ to $1/T^6$, the equation is (Polyakov and Mineev 2000; Polyakov et al. 2005; Dauphas et al. 2018):

$$\ln\beta_{I/I^*} = \left[\frac{3}{40}\left(\frac{\theta_D}{T}\right)^2 - \frac{1}{1120}\left(\frac{\theta_D}{T}\right)^4 + \frac{1}{60480}\left(\frac{\theta_D}{T}\right)^6\right] \times \left(\frac{M - M^*}{M^*}\right) \quad (10)$$

where I and I^* are two isotopes of masses M and M^*, and θ_D is the Debye temperature calculated from Equation 9. Using Equations 9 and 10, we calculate the equilibrium fractionation factor between ^{57}Fe and ^{54}Fe at different pressures and temperatures (Fig. 4). The β-factor between ^{57}Fe and ^{54}Fe of pure iron at room pressure is calculated using the f_{LM} data of α-iron up to the α−γ transition temperature from Mauger et al. (2014) (Fig. 4a). The β-factor of iron at ~50 GPa is calculated from our measured f_{LM} data of γ- and ε-Fe, and the f_{LM} is calculated from the 50 GPa FLMT model (Fig. 4b). At the melting point, f_{LM} is zero, and the value of $\langle u^2\rangle$ in Equation 9 diverges in the FLMT model.

Using a quasiharmonic Debye model, our data clearly shows that at high temperatures, the equilibrium isotopic fractionation $\ln\beta^{57/54}_{Fe}$ is systematically lower than the results extrapolated from room-temperature NRIXS data using the GM approach (Fig. 4), which is supported by published data (see "Support of the quasiharmonic correction from published data" section below). In several recent studies that utilized the GM approach, the $\ln\beta^{57/54}_{Fe}$ was calculated from force constants that were derived from room temperature NRIXS spectra, and these force constants were assumed to be invariant with temperature (e.g., Dauphas et al. 2012; Shahar et al. 2016; Liu et al. 2017). Our calculation suggests that the quasiharmonic correction would systematically lower the $\ln\beta^{57/54}_{Fe}$ between 1600 and 2800 K at 50 GPa by ~0.1‰ when compared to the $\ln\beta^{57/54}_{Fe}$ calculated at high temperature using a room temperature force constant, thus indicating the force constant varies with temperature.

Support of the quasiharmonic correction from published data

Quasiharmonic correction of mantle and core materials constrained from macroscopic thermodynamic quantities

Polyakov (1998, 2009) consider various temperature effects to the calculations of the isotope fractionation β-factor and suggest that intrinsic anharmonicity has a minor effect on the β-factor (Polyakov 1998). Therefore, Polyakov (2009) evaluates the effects of temperature using the approach of Gillet et al. (1996), but neglects the intrinsically anharmonic term (Polyakov 1998), and provides an estimate to the quasiharmonic correction to the β-factor using the following equation:

$$\frac{\Delta\ln\beta}{\ln\beta} = -\frac{6\gamma\gamma_{th}RT}{VK_T} \quad (11)$$

where γ is the normalized modal Grüneisen parameter, γ_{th} is the thermal Grüneisen parameter, which is equal to γ for single-element substances (e.g., Fe), R is the gas constant, V is the molar volume, and K_T is the isothermal bulk modulus. Equation 11 uses thermodynamic parameters that cover the whole phonon spectrum and is not limited by the Debye model where a cut-off phonon energy exists (Polyakov 1998). Using updated thermodynamic

parameters, we recalculate the quasiharmonic corrections to the β-factor of iron at high temperatures using Equation 11. For α-Fe at 1000 K and 1 bar, we use γ = 1.81 (Mauger et al. 2014), V = 7.32 cm^3/mol (Liu et al. 2004), and K_T = 139.1 GPa (Dever 1972). The estimated quasiharmonic correction of α-Fe at 1000 K is –0.12‰. For comparison, Polyakov (2009) estimated the upper bound of the quasiharmonic correction to $\ln\beta_{Fe}^{57/54}$ as ~–0.03‰ at 1000 K (1 bar) by assuming V_{Fe} = 6.89 cm^3/mol and a Grüneisen parameter γ = 1.

For ε-Fe at 50 GPa and 3000 K, we use γ = 1.65 (Murphy et al. 2011), V = 5.56 cm^3/mol (Murphy et al. 2011), and K_T = 240 GPa (Fei et al. 2016). The estimated quasiharmonic correction of ε-Fe at 50 GPa and 3000 K is –0.05‰. The Grüneisen parameters used in the recalculation are extrapolated from room-temperature NRIXS results and could introduce an estimated uncertainty of up to 15% [estimated from the variation in Grüneisen parameters of ε-Fe (Merkel et al. 2000; Lübbers et al. 2000; Giefers et al. 2002; Murphy et al. 2011)], which leads to a propagated uncertainty of 0.02‰ to $\ln\beta_{Fe}^{57/54}$ in the quasiharmonic correction. The quasiharmonic corrections to $\ln\beta_{Fe}^{57/54}$ of α- and ε-Fe using Equation 11 are compatible with our estimations shown in Figure 4 (–0.10 ± 0.02‰), and the quasiharmonic corrections constrained by both methods have consistent and appropriate direction. One advantage of our approach is that the experiment is carried out in situ at high-P-T conditions.

Published data revisited: Does the general moment's method capture the quasiharmonic correction?

The GM model can be derived either using the Bigeleisen-Mayer-Urey equation or using an alternative approach from the kinetic energy (Bigeleisen and Mayer 1947; Urey 1947; Polyakov 1998, 2009; Dauphas et al. 2012). The Bigeleisen-Mayer-Urey equation is compatible with both harmonic and quasiharmonic Debye models (Polyakov 1998) and is approximated by the GM model using the phonon DOS when expanded in Taylor series (Kowalski and Jahn 2011). In order for the GM model to be valid to approximate the Bigeleisen-Mayer-Urey equation, it is required that the phonon angular frequencies ω (cm^{-1}) < 8.73 T(K) (Kowalski and Jahn 2011)[1]. The vibrational angular frequency of iron in minerals is usually less than 1000 cm^{-1} (Dauphas et al. 2012), so the GM model can be used to calculate the β-factor at temperatures above 115 K. Therefore, it is possible to validate the β-factor calculated from f_{LM} with the GM model using phonon DOS measurements at high temperatures.

We examined published DOS data that were collected at both room pressure and high pressures from other research groups (Mauger et al. 2014; Lin et al. 2005). In the validation with the room-pressure data, we used the f_{LM} and the phonon DOS that come from the same NRIXS data set to calculate the β-factor (Mauger et al. 2014). We calculated the β-factor from the f_{LM} using Equations 9 and 10, and we calculated the β-factor from the high-temperature phonon DOS using the equations from the GM approach given in Polyakov (2009) and Dauphas et al. (2018). Figure 5 demonstrates that the β-factors calculated from the same high-temperature NRIXS data set using different approaches are consistent with each other. Figure 4a shows that the lnβ calculated from both the f_{LM} (cyan squares, Fig. 4a) and the phonon DOS (magenta crosses, Fig. 4a) are lower than the

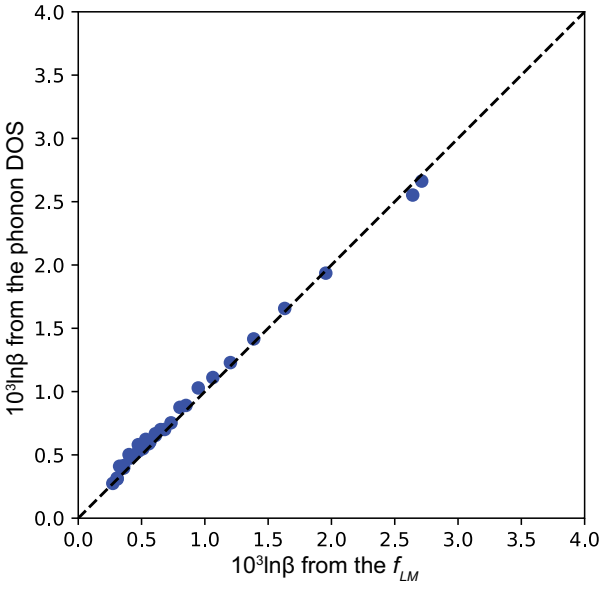

Figure 5. Equilibrium isotope fractionation β-factor between ^{57}Fe and ^{54}Fe at ambient pressure, determined from f_{LM} (horizontal axis, this study) and the phonon DOS (vertical axis). Both the f_{LM} and the phonon DOS are from Mauger et al. (2014). Black dashed line: Y = X identity line. (Color online.)

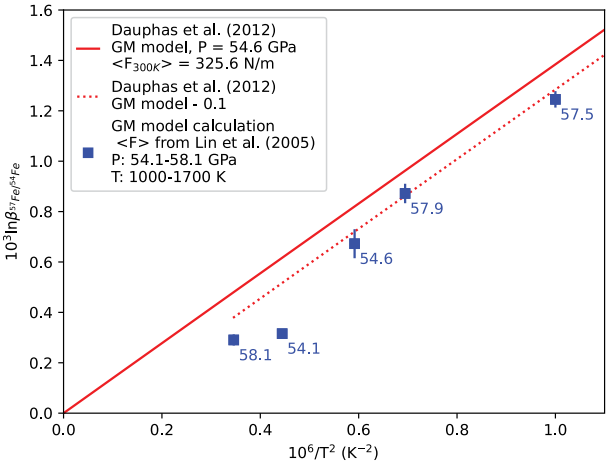

Figure 6. Equilibrium isotope fractionation β-factor between ^{57}Fe and ^{54}Fe in ε-Fe at simultaneous high-P-T conditions calculated using GM method (Dauphas et al. 2012). Red solid line = $\ln\beta_{Fe}^{57/54}$ calculated from GM model using force constant determined at 54.6 GPa and 300 K (325.6 N/m) (Dauphas et al. 2012). Red dotted line = $\ln\beta_{Fe}^{57/54}$ calculated from GM model shifted down by 0.1‰ for the purpose of demonstration, truncated at 1700 K since experimental data above 1700 K is unavailable. Blue squares = $\ln\beta_{Fe}^{57/54}$ calculated from GM model using force constants measured at simultaneous high-P-T conditions from Lin et al. (2005). Coefficient B_2 from the Table 1 in Dauphas et al. (2012) is used in the calculation, and the blue number next to each data point indicates the pressure of each measurement. The lnβ calculated from the GM model using simultaneous high-P-T force constant is systematically lower than the lnβ extrapolated from the GM model using room temperature force constant by at least 0.1‰. (Color online.)

extrapolation of GM model using the phonon DOS collected at ambient temperature by about 0.1‰. Taken together, the results shown in Figures 4 and 5 suggest that the β-factor computed from NRIXS spectra collected at high temperatures and/or phonon DOS collected at high temperatures leads to a more consistent result than the β-factor extrapolated to high temperatures using the force constant derived from room-temperature data.

While most published high-temperature β-factors calculated from the GM model were extrapolated from room temperature phonon DOS and/or force constants, Lin et al. (2005) measured the phonon DOS of ε-Fe at simultaneous high-*P*-*T* conditions and reported the associated force constants, which are used to compare with the β-factors of ε-Fe determined by our approach. Figure 6 demonstrates the lnβ of ε-Fe calculated from the GM method using force constants collected at simultaneous high-*P*-*T* conditions (Lin et al. 2005) are at least 0.1‰ lower than the extrapolation of the GM model using a force constant collected at room temperature (54.6 GPa, 325.6 N/m, Dauphas et al. 2012), consistent with the quasiharmonic correction that we have observed with our approach. Our conclusion is that the GM method would capture the quasiharmonic corrections to the β-factor when the phonon DOS or force constants collected at high temperatures are used.

Discussion on the effect of phase transitions and pressure uncertainty

Phase transitions

In this section, we discuss reasons why the (lnβ, $10^6/T^2$) trend does not necessarily have to intercept the $10^6/T^2$ axis at (0, 0). The point (0, 0) in the (lnβ, $10^6/T^2$) space does not hold physical significance. The material presented in this study (solid Fe), and similar to all materials, is characterized by phase transitions with increasing temperature and an intercept of (0, 0) from the extrapolation of the (lnβ, $10^6/T^2$) plot of the solid phase would neglect such phase transitions. Our results show that for the solid Fe phases, the (lnβ, $10^6/T^2$) trend does not intercept the (0, 0) point. Rather, the intercept of (lnβ, $10^6/T^2$) trend on the $10^6/T^2$ axis corresponds to a temperature higher than the melting point (see below), i.e., the solid phase never reaches it. For $T\rightarrow\infty$, a liquid will turn into either a gas (below the critical pressure) or a supercritical state (above the critical pressure). The temperature dependence of lnβ in the high-temperature phases (liquid, gas, or supercritical) is generally unknown, except for a classical monatomic ideal gas (see below).

As Polyakov (1997) and Dauphas et al. (2018) have pointed out, lnβ is related to the average atomic kinetic energy (*KE*) based on the following equation:

$$\ln\beta = \frac{\Delta m}{m^*}\left(\frac{KE}{k_B T} - \frac{3}{2}\right) \quad (12)$$

where Δm is the mass difference between two isotopes, m^* is the atomic mass of the element, and k_B is the Boltzmann constant. In order for lnβ = 0, one only needs $KE = 3/2\ k_B T$, which coincides with the average atomic kinetic energy of the classical monatomic ideal gas (Landau and Lifshitz 1980). Therefore, the lnβ of a classical monatomic ideal gas is 0, which is the reason why the β-factor is defined as the isotope fractionation factor between the material of interest and a classical monatomic ideal gas reference (e.g., Richet et al. 1977; Schauble 2011; Huang et al. 2013; Eldridge et al. 2016).

Here we discuss two scenarios:

(1) 1 bar. Fe has a sharp liquid-gas phase boundary and a well-defined gaseous phase at ambient pressure (boiling point 3273 K; Zhang et al. 2011). Evaporation experiments have demonstrated that Fe vapor behaves as a classical monatomic gas (Safarian and Engh 2013). Based on the discussion above, we predict that lnβ of Fe would be equal to 0 at temperatures above its 1 bar boiling point. To validate our prediction, we extrapolate (lnβ, $10^6/T^2$) of the data calculated from the f_{LM} and DOS data from Mauger et al. (2014) to high temperatures using a linear model, and the linear extrapolations intercept the $10^6/T^2$ axis at temperatures of 3292 K (f_{LM}) and 4492 K (DOS) (please refer to the Online Materials[2]). Both temperatures are above the 1 bar boiling point of Fe but below infinity.

(2) 50 GPa. The critical pressure of Fe is estimated at ~1 GPa (Ray et al. 2006), so Fe is unlikely to transition into a well-defined gaseous phase at 50 GPa. Instead Fe will likely go into the supercritical phase at high enough temperatures (Landau and Lifshitz 1980). The linear extrapolation of (lnβ, $10^6/T^2$) derived from the f_{LM} from our study intercepts the $10^6/T^2$ axis at a temperature of 3469 K. To our knowledge, no study has constrained the supercritical transition temperature for Fe at 50 GPa, so it is challenging to benchmark this value. We expect that the harmonic model provides the highest possible bound for lnβ above the melting point of Fe, and the actual lnβ value is expected to be lower than the harmonic model (because the quasiharmonic correction would lower the lnβ, Fig. 4b).

Pressure uncertainty

Murphy et al. (2013) determined the force constant of ε-Fe at ambient temperature and high pressures from the integrated phonon DOS. The pressure derivative of the force constant for ε-Fe is 2.124 N/(m·GPa), and the projected force constants at 50 and 55 GPa are 293 and 304 N/m, respectively. If we neglect the quasiharmonic correction and focus only on the intrinsic pressure effect, at 3000 K and 50 GPa, lnβ = 0.139‰; and at 3000 K and 55 GPa, lnβ = 0.144‰, resulting in a Δlnβ of 0.005‰. We carried out similar calculations with the force constant data from Shahar et al. (2016) reported at 17 and 40 GPa, which are derived from the moments of the refined NRIXS spectra. The pressure derivative of the force constant for ε-Fe from Shahar et al. (2016) is 2.786 N/(m·GPa), resulting in a Δlnβ of 0.007‰ between 50 and 55 GPa at 3000 K. The Δlnβ that is intrinsically because of the pressure effect [0.005‰ based on Murphy et al. (2013) or 0.007‰ based on Shahar et al. (2016)] is more than one order of magnitude smaller than the estimated quasiharmonic correction (0.1‰). The effect of the pressure uncertainty on the lnβ is, therefore, minor compared to the quasiharmonic correction at temperatures relevant to the core-formation scenario, and the pressure uncertainty would not yield an intercept at (0, 0) for the (lnβ, $10^6/T^2$) trend.

Implications

Our result demonstrates that the lattice vibrations of iron at high-*P*-*T* conditions deviates from harmonicity. One implication of our finding is to incorporate these results into studies involv-

ing iron isotope fractionation, such as the core formation process. Geochemical studies have demonstrated that mantle-derived rocks are ~0.1‰ heavier in δ^{57}Fe than rocks from Mars and Vesta, which are believed to have chondritic δ^{57}Fe value (Poitrasson et al. 2004; Sossi et al. 2016). Based on NRIXS measurements and a proposed quasiharmonic correction, Polyakov (2009) suggests that the core-mantle differentiation would leave an imprint on the iron isotope composition of the mantle rocks. However, based on the harmonic extrapolation from recent high pressure, room-temperature NRIXS measurements where a quasiharmonic correction is neglected, the isotope fractionation between metallic iron and silicates at core formation conditions (~40–60 GPa, ~3000 K) is expected to be smaller than 0.1‰.

Yang et al. (2019) determine the force constant of Fe in bridgmanite with a composition of $Mg_{0.92}Fe_{0.09}Si_{0.99}O_3$ as 322.7 ± 28.0 N/m at 50 GPa and 300 K, and the same group determine the force constant of Fe in ferropericlase with a composition of $Mg_{0.75}Fe_{0.25}O$ as 333.1 ± 17.6 N/m at 54 GPa and 300 K. If one neglects the quasiharmonic correction and calculates the high-temperature $\ln\beta_{Fe}^{57/54}$ from room temperature force constants, the $\ln\beta_{Fe}^{57/54}$ is 0.153 ± 0.013‰ for bridgmanite and 0.158 ± 0.008‰ for ferropericlase at 3000 K. The force constant of Fe in ε-Fe varies between different studies. If one takes an average of the force constants measured between 50 and 55 GPa from Lin et al. (2005) and Murphy et al. (2013), the averaged force constant in ε-Fe is 309 ± 11 N/m at 53 GPa and 300 K, which corresponds to a $\ln\beta_{Fe}^{57/54}$ of 0.147 ± 0.005‰ at 3000 K without a quasiharmonic correction. If the quasiharmonic correction is neglected, the difference in $\ln\beta_{Fe}^{57/54}$ between Fe and mantle materials at ~50 GPa and 3000 K is in the order of 0.01‰. Using phonon DOS calculated from density functional theory, Shahar et al. (2016) calculate the iron isotopic fractionation between bridgmanite and iron ($\Delta^{57}Fe_{Brg-Fe} = \delta^{57}Fe_{Brg} - \delta^{57}Fe_{Fe} = \ln\beta_{Fe}^{57/54}Fe - \ln\beta_{Fe}^{57/54}Fe$) at 60 GPa and ~3500 K as 0.02–0.04‰. Using basaltic glass as a proxy for mantle melts, Liu et al. (2017) calculate $\Delta^{56}Fe_{mantle\text{-}Fe}$ at 40–60 GPa and 3000–4000 K as 0–0.02‰, which is equivalent to a $\Delta^{57}Fe_{mantle\text{-}Fe}$ of 0–0.03‰ if one recalculates the δ^{57} Fe using the same force constant as δ^{56}Fe. Both studies conclude that the core formation process is unlikely to leave an iron isotopic fingerprint on mantle rocks. However, if quasiharmonic correction is considered, there may be an observable effect, as discussed below.

We now consider rough estimates of the quasiharmonic correction to the β-factor of lower mantle minerals using Equation 11. Wolf et al. (2015) measured the thermal equation of state of iron-bearing bridgmanite and thus provide constraints on all the parameters in Equation 11; in this case, one needs to assume that the normalized modal Grüneisen parameter γ of iron in bridgmanite is the same as its thermal Grüneisen parameter, which is yet to be tested. At 50 GPa and 3000 K, the thermal Grüneisen parameter γ_{th} for iron-bearing bridgmanite is 1.3, the isothermal bulk modulus is 370.6 GPa, and molar volume is 24.6 cm^3/mol (Wolf et al. 2015). Using Equation 11, the estimated quasiharmonic correction to $\ln\beta_{Fe}^{57/54}$ in bridgmanite is –0.006‰. If we now use this estimated quasiharmonic correction to β-factors in bridgmanite and the quasiharmonic correction in metallic iron determined from this study (–0.1‰), the core formation process, modeled as $\Delta^{57}Fe_{Brg\text{-}Fe}$, would leave an isotopic fingerprint of 0.09–0.13‰. This $\Delta^{57}Fe_{Brg\text{-}Fe}$ value is close to the δ^{57} Fe compared between mantle-derived rocks and chondrites (~0.1‰) (Poitrasson et al. 2004; Wang et al. 2012; Sossi et al. 2016). For ferropericlase, the other major Fe-bearing major phase in the lower mantle, the reported thermoelastic parameters at 50 GPa and 3000 K are: V = 10.4 cm^3/mol (Mao et al. 2011), K_T = 292.0 GPa (Mao et al. 2011), and γ = 1.3 (Fischer et al. 2011). Based on Equation 11, the estimated quasiharmonic correction to $\ln\beta_{Fe}^{57/54}$ in ferropericlase is –0.013‰, which is also significantly smaller than that for the metallic Fe phase (–0.1‰) and will not change the conclusion that ^{57}Fe preferentially partitions into these lower-mantle phases when considering quasiharmonic behavior.

The exact fraction of the equilibrium δ^{57}Fe that would be transferred to the mantle depends on the mass ratio of iron between the metallic phase and the mantle phases in the core-formation process. If we assume that 90% of the iron is in the core, based on the lever rule [$\delta^{57}Fe_{mantle} = (\delta^{57}Fe_{Earth} - \delta^{57}Fe_{core}f_{core}^{Fe})/(1 - f_{core}^{Fe})$; $\delta^{57}Fe_{mantle} - \delta^{57}Fe_{core}$ = 0.1‰] the calculated $\delta^{57}Fe_{mantle}$ is 0.09‰. This $\delta^{57}Fe_{mantle}$ value is close to the δ^{57} Fe compared between mantle-derived rocks and chondrites (~0.1‰) (Poitrasson et al. 2004; Wang et al. 2012; Sossi et al. 2016). Our conclusion is that one cannot rule out the possibility that the process of core formation would leave the mantle enriched with heavier iron isotopes compared to chondrites (Poitrasson et al. 2004; Weyer et al. 2005; Schoenberg and von Blanckenburg 2006).

Concluding remarks

We constrain the mean-square displacement of the iron atoms by measuring the f_{LM} of γ- and ε-Fe at pressures around 50 GPa and temperatures above 1650 K using synchrotron Mössbauer spectroscopy. This approach avoids the difficulty in maintaining stable and uniform high sample temperatures for hours, a requirement in conventional Mössbauer and NRIXS measurements. Extrapolation of our results to 300–1700 K, where previous measurements have been conducted, shows good agreement, suggesting that the f_{LM} captures the behavior of the phonons in iron metal reasonably well.

We find that the f_{LM} is more sensitive to temperature than to pressure, and the temperature dependence for γ- and ε-Fe varies continuously up to melting within the experimental uncertainties. At the pressures investigated here (around 50 GPa), the f_{LM} of iron has a linear temperature dependence.

We establish the relationship between f_{LM}, the lattice vibrations of iron, and iron isotope fractionation. We assume weak anharmonicity, which permits us to use a quasiharmonic Debye model for the lattice vibrations. We calculate the Debye temperatures of the γ- and ε-Fe at elevated pressure-temperature conditions from this model. From the calculated Debye temperatures, the equilibrium isotopic fractionation β-factors of iron at high pressures and high temperatures are computed. Our result is consistent with the β-factors determined by previous NRIXS studies at relatively low temperature (T < 600 K). However, for the high-temperature data (T > 600 K), we find that the quasiharmonic correction is significant enough to have an observable isotopic effect. Calculations based on our experimental data (around 50 GPa, 1600–2800 K) demonstrate that the quasiharmonic correction would lower $\ln\beta_{Fe}^{57/54}$ by 0.1‰ compared to the extrapolation of room temperature NRIXS results. The offset of 0.1‰ in $\ln\beta_{Fe}^{57/54}$ is enough to account for the observed δ^{57} Fe in mantle rocks compared to chondrites. Therefore, it is plausible that core formation processes left an observable iron isotopic signature in mantle rocks. Our experi-

mental results on hot compressed iron highlight the importance of considering nonharmonic effects to the evaluation of isotopic fractionation β-factors in minerals at deep Earth conditions.

Acknowledgments

The authors thank Thomas S. Toellner for his help with the experiments. We also thank Lisa Mauger for kindly providing the published phonon DOS of α-Fe from her paper. The authors acknowledge Veniamin B. Polyakov, Aleksandr Chumakov, and Paolo Sossi for their thoughtful, thorough and constructive comments, which helped to improve our manuscript.

Funding

We thank the National Science Foundation (EAR-CSEDI-1316362, EAR-CSEDI-2009935, and EAR-1727020) for support of this research. Use of the Advanced Photon Source is supported by the Department of Energy, Office of Science (DE-AC02-06CH11357). Sector 3 operations are supported in part by COMPRES under National Science Foundation Cooperative Agreement EAR-1661511. We thank GeoSoilEnviroCARS (NSF EAR-1634415 and DOE DE-FG02-94ER14466) for the help with sample preparation. D.Z. acknowledges the Argonne Graduate Research Program to support part of this research.

References cited

Alfè, D., Gillan, M., and Price, G. (1999) The melting curve of iron at the pressures of the Earth's core from ab initio calculations. Nature, 401, 462–464.

——— (2002) Composition and temperature of the Earth's core constrained by combining ab initio calculations and seismic data. Earth and Planetary Science Letters, 195, 91–98.

Alfè, D., Vo Adlo, L., Price, G.D., and Gillan, M.J. (2004) Melting curve of materials: Theory versus experiments. Journal of Physics: Condensed Matter, 16, S973–S982.

Allen, P.B. (2020) Theory of thermal expansion: Quasi-harmonic approximation and corrections from quasi-particle renormalization. Modern Physics Letters B, 34, 2050025.

Anzellini, S., Dewaele, A., Mezouar, M., Loubeyre, P., and Morard, G. (2013) Melting of iron at Earth's inner core boundary based on fast X-ray diffraction. Science, 340(6131), 464–466.

Bansal, D., Aref, A., Dargush, G., and Delaire, O. (2016) Modeling non-harmonic behavior of materials from experimental inelastic neutron scattering and thermal expansion measurements. Journal of Physics: Condensed Matter, 28, 385201.

Baroni, S., Giannozzi, P., and Isaev, E. (2010) Density-functional perturbation theory for quasi-harmonic calculations. Reviews in Mineralogy and Geochemistry, 71, 39–57.

Bergmann, U., Shastri, S.D., Siddons, D.P., Batterman, B.W., and Hastings, J.B. (1994) Temperature dependence of nuclear forward scattering of synchrotron radiation in α-^{57}Fe. Physical Review. B, Condensed Matter, 50, 5957–5961.

Bigeleisen, J., and Mayer, M.G. (1947) Calculation of equilibrium constants for isotopic exchange reactions. The Journal of Chemical Physics, 15, 261–267.

Blanco, M.A., Francisco, E., and Luaña, V. (2004) Gibbs: Isothermal-isobaric thermodynamics of solids from energy curves using a quasi-harmonic Debye model. Computer Physics Communications, 158, 57–72.

Boyle, A.J.F., Bunbury, D.S.P., Edwards, C., and Hall, H.E. (1961) The Mössbauer effect in tin from 120 K to the melting point. Proceedings of the Physical Society, 77, 129–135.

Brown, J.S. (1969) Anharmonic effects on the Mössbauer recoilless fraction of solid krypton. Physical Review, 187, 401–402.

Chai, M., Brown, J.M., and Slutsky, L.J. (1996) Thermal diffusivity of mantle minerals. Physics and Chemistry of Minerals, 23, 470–475.

Chen, B., Li, Z., Zhang, D., Liu, J., Hu, M.Y., Zhao, J., Bi, W., Alp, E.E., Xiao, Y., Chow, P., and Li, J. (2014) Hidden carbon in Earth's inner core revealed by shear softening in dense Fe_7C_3. Proceedings of the National Academy of Sciences, 111, 17755–17758.

Chumakov, A.I., and Sturhahn, W. (1999) Experimental aspects of inelastic nuclear resonance scattering. Hyperfine Interactions, 123/124, 781–808.

Chumakov, A.I., Rüffer, R., Baron, A.Q.R., Grünsteudel, H., and Grünsteudel, H.F. (1996) Temperature dependence of nuclear inelastic absorption of synchrotron radiation in α-^{57}Fe. Physical Review B, 54, R9596–R9599.

Dauphas, N., Roskosz, M., Alp, E.E., Golden, D.C., Sio, C.K., Tissot, F.L.H., Hu, M.Y., Zhao, J., Gao, L., and Morris, R.V. (2012) A general moment NRIXS approach to the determination of equilibrium Fe isotopic fractionation factors: Application to goethite and jarosite. Geochimica et Cosmochimica Acta, 94, 254–275.

Dauphas, N., Hu, M.Y., Baker, E.M., Hu, J., Tissot, F.L.H., Alp, E.E., Roskosz, M., Zhao, J., Bi, W., Liu, J., Lin, J.-F., Nie, N.X., and Heard, A. (2018) SciPhon: A data analysis software for nuclear resonant inelastic X-ray scattering with applications to Fe, Kr, Sn, Eu and Dy. Journal of Synchrotron Radiation, 25, 1581–1599.

Debye, P. (1913) Uber die intensitatsverteilung in den mit rontgenstrahlen erzeugten interferenzbildern. Verhandlungen Der Deutschen Physikalischen Gesellschaft, 15, 738–752.

Dever, D. (1972) Temperature dependence of the elastic constants in α-iron single crystals: relationship to spin order and diffusion anomalies. Journal of Applied Physics, 43, 3293–3301.

Dunitz, J.D., Schomaker, V., and Trueblood, K.N. (1988) Interpretation of atomic displacement parameters from diffraction studies of crystals. The Journal of Physical Chemistry, 92, 856–867.

Eldridge, D.L., Guo, W., and Farquhar, J. (2016) Theoretical estimates of equilibrium sulfur isotope effects in aqueous sulfur systems: Highlighting the role of isomers in the sulfite and sulfoxylate systems. Geochimica et Cosmochimica Acta, 195, 171–200.

Erba, A. (2014) On combining temperature and pressure effects on structural properties of crystals with standard ab initio techniques. The Journal of Chemical Physics, 141, 124115.

Fei, Y., Murphy, C., Shibazaki, Y., Shahar, A., and Huang, H. (2016) Thermal equation of state of hcp-iron: Constraint on the density deficit of Earth's solid inner core. Geophysical Research Letters, 43, 6837–6843.

Fischer, R.A., Campbell, A.J., Shofner, G.A., Lord, O.T., Dera, P., and Prakapenka, V.B. (2011) Equation of state and phase diagram of FeO. Earth and Planetary Science Letters, 304, 496 –502.

Fultz, B. (2010) Vibrational thermodynamics of materials. Progress in Materials Science, 55, 247–352.

Giefers, H., Lübbers, R., Rupprecht, K., Wortmann, G., Alfè, D., and Chumakov, A.I. (2002) Phonon spectroscopy of oriented hcp iron. High Pressure Research, 22, 501–506.

Gillet, P., McMillan, P., Schott, J., Badro, J., and Grzechnik, A. (1996) Thermodynamic properties and isotopic fractionation of calcite from vibrational spectroscopy of ^{18}O-substituted calcite. Geochimica et Cosmochimica Acta, 60, 3471–3485.

Henke, B.L., Gullikson, E.M., and Davis, J.C. (1993) X-ray interactions: Photoabsorption, scattering, transmission, and reflection at E=50–30000 eV, Z=1–92. Atomic Data and Nuclear Data Tables, 54, 181–342.

Huang, F., Chen, L., Wu, Z., and Wang, W. (2013) First-principles calculations of equilibrium mg isotope fractionations between garnet, clinopyroxene, orthopyroxene, and olivine: Implications for mg isotope thermometry. Earth and Planetary Science Letters, 367, 61–70.

Jackson, J.M., Sturhahn, W., Lerche, M., Zhao, J., Toellner, T.S., Alp, E.E., Sinogeikin, S.V., Bass, J.D., Murphy, C.A., and Wicks, J.K. (2013) Melting of compressed iron by monitoring atomic dynamics. Earth and Planetary Science Letters, 362, 143–150.

Jeanloz, R., and Morris, S. (1986) Temperature distribution in the crust and mantle. Annual Review of Earth and Planetary Sciences, 14, 377–415.

Jeanloz, R., and Richter, F.M. (1979) Convection, composition, and the thermal state of the lower mantle. Journal of Geophysical Research, 84, 5497–5504.

Kieffer, S.W. (1979a) Thermodynamics and lattice vibrations of minerals: 1. mineral heat capacities and their relationships to simple lattice vibrational models. Reviews of Geophysics, 17, 1–19.

——— (1979b) Thermodynamics and lattice vibrations of minerals: 2. vibrational characteristics of silicates. Reviews of Geophysics, 17, 20–34.

——— (1979c) Thermodynamics and lattice vibrations of minerals: 3. Lattice dynamics and an approximation for minerals with application to simple substances and framework silicates. Reviews of Geophysics, 17, 35–59.

——— (1980) Thermodynamics and lattice vibrations of minerals: 4. Application to chain and sheet silicates and orthosilicates. Reviews of Geophysics, 18, 862–886.

——— (1982) Thermodynamics and lattice vibrations of minerals: 5. Applications to phase equilibria, isotopic fractionation, and high-pressure thermodynamic properties. Reviews of Geophysics, 20, 827–849.

Kim, D.S., Hellman, O., Herriman, J., Smith, H.L., Lin, J.Y.Y., Shulumba, N., Niedziela, J.L., Li, C.W., Abernathy, D.L., and Fultz, B. (2018) Nuclear quantum effect with pure anharmonicity and the anomalous thermal expansion of silicon. Proceedings of the National Academy of Sciences, 115, 1992–1997.

Kolk, B., Bleloch, A.L., and Hall, D.B. (1986) Recoilless fraction studies of iron near the curie temperature. Hyperfine Interactions, 29, 1377–1380.

Komabayashi, T., and Fei, Y. (2010) Internally consistent thermodynamic database for iron to the Earth's core conditions. Journal of Geophysical Research, 115, 252–257.

Komabayashi, T., Fei, Y., Meng, Y., and Prakapenka, V.B. (2009) In-situ X-ray diffraction measurements of the γ−ε transition boundary of iron in an internally-heated diamond anvil cell. Earth and Planetary Science Letters, 282, 252–257.

Kovats, T.A., and Walker, J.C. (1969) Mössbauer absorption in Fe^{57} in metallic iron from the curie point to the γ-δ transition. Physical Review, 181, 610–618.

Kowalski, P.M., and Jahn, S. (2011) Prediction of equilibrium Li isotope fractionation between minerals and aqueous solutions at high *P* and *T*: An efficient ab initio approach. Geochimica et Cosmochimica Acta, 75, 6112–6123.

Landau, L., and Lifshitz, E. (1980) Statistical Physics, 3rd ed., Part I. Pergamon.

Leu, B.M., and Sage, J.T. (2016) Stiffness, resilience, compressibility. Hyperfine Interactions, 237, 87.

Lin, J.-F., Sturhahn, W., Zhao, J., Shen, G., Mao, H.-K., and Hemley, R.J. (2005) Sound velocities of hot dense iron: Birch's law revisited. Science, 308, 1892–1894.

Liu, Y., Sommer, F., and Mittemeijer, E. (2004) Calibration of the differential dilatometric measurement signal upon heating and cooling; Thermal expansion of pure iron. Thermochimica Acta, 413, 215–225.

Liu, J., Dauphas, N., Roskosz, M., Hu, M.Y., Yang, H., Bi, W., Zhao, J., Alp, E.E., Hu, J.Y., and Lin, J.-F. (2017) Iron isotopic fractionation between silicate mantle and metallic core at high pressure. Nature Communications, 8, 14377.

Lübbers, R., Grünsteudel, H.F., Chumakov, A.I., and Wortmann, G. (2000) Density of phonon states in iron at high pressure. Science, 287, 1250–1253.

Macedo, W.A.A., and Keune, W. (1988) Magnetism of epitaxial fcc-Fe(100) films on Cu(100) investigated in situ by conversion-electron Mössbauer spectroscopy in ultrahigh vacuum. Physical Review Letters, 61, 475–478.
Mao, Z., Lin, J.-F., Liu, J., and Prakapenka, V.B. (2011) Thermal equation of state of lower-mantle ferropericlase across the spin crossover. Geophysical Research Letters, 38.
Mauger, L., Lucas, M.S., Muñoz, J.A., Tracy, S.J., Kresch, M., Xiao, Y., Chow, P., and Fultz, B. (2014) Nonharmonic phonons in α-iron at high temperatures. Physical Review B, 90, 064303.
Merkel, S., Goncharov, A.F., Mao, H.K., Gillet, P., and Hemley, R.J. (2000) Raman spectroscopy of iron to 152 gigapascals: Implications for Earth's inner core. Science, 288, 1626–1629.
Morrison, R.A., Jackson, J.M., Sturhahn, W., Zhao, J., and Toellner, T.S. (2019) High pressure thermoelasticity and sound velocities of Fe-Ni-Si alloys. Physics of the Earth and Planetary Interiors, 294, 106268.
Murphy, C.A., Jackson, J.M., Sturhahn, W., and Chen, B. (2011) Grüneisen parameter of hcp-Fe to 171 GPa. Geophysical Research Letters, 38.
Murphy, C.A., Jackson, J.M., and Sturhahn, W. (2013) Experimental constraints on the thermodynamics and sound velocities of hcp-Fe to core pressures. Journal of Geophysical Research: Solid Earth, 118, 1999–2016.
Poitrasson, F., Halliday, A.N., Lee, D.-C., Levasseur, S., and Teutsch, N. (2004) Iron isotope differences between Earth, Moon, Mars and Vesta as possible records of contrasted accretion mechanisms. Earth and Planetary Science Letters, 223, 253–266.
Polyakov, V.B. (1997) Equilibrium fractionation of the iron isotopes: Estimation from Mössbauer spectroscopy data. Geochimica et Cosmochimica Acta, 61, 4213–4217.
——— (1998) On anharmonic and pressure corrections to the equilibrium isotopic constants for minerals. Geochimica et Cosmochimica Acta, 62, 3077–3085.
——— (2009) Equilibrium iron isotope fractionation at core-mantle boundary conditions. Science, 323, 912–914.
Polyakov, V.B., and Mineev, S.D. (2000) The use of Mössbauer spectroscopy in stable isotope geochemistry. Geochimica et Cosmochimica Acta, 64, 849 –865.
Polyakov, V., Mineev, S., Clayton, R., Hu, G., Gurevich, V., Khramov, D., Gavrichev, K., Gorbunov, V., and Golushina, L. (2005) Oxygen isotope fractionation factors involving cassiterite (sno2): I. Calculation of reduced partition function ratios from heat capacity and X-ray resonant studies. Geochimica et Cosmochimica Acta, 69, 1287–1300.
Polyakov, V.B., Clayton, R.N., Horita, J., and Mineev, S.D. (2007) Equilibrium iron isotope fractionation factors of minerals: Reevaluation from the data of nuclear inelastic resonant X-ray scattering and Mössbauer spectroscopy. Geochimica et Cosmochimica Acta, 71, 3833–3846.
Prescher, C., and Prakapenka, V.B. (2015) DIOPTAS: A program for reduction of two-dimensional X-ray diffraction data and data exploration. High Pressure Research, 35, 223–230.
Ray, A., Srivastava, M., Kondayya, G., and Menon, S. (2006) Improved equation of state of metals in the liquid-vapor region. Laser and Particle Beams, 24, 437–445.
Reynard, B., Caracas, R., and McMillan, P. (2015) Lattice vibrations and spectroscopy of mantle phases. In G. Schubert, Ed., Treatise on Geophysics (2nd ed.), 203– 231. Elsevier.
Richet, P., Bottinga, Y., and Javoy, M. (1977) A review of hydrogen, carbon, nitrogen, oxygen, sulphur, and chlorine stable isotope fractionation among gaseous molecules. Annual Review of Earth and Planetary Sciences, 5, 65–110.
Safarian, J., and Engh, T.A. (2013) Vacuum evaporation of pure metals. Metallurgical and Materials Transactions A, 44, 747–753.
Schauble, E.A. (2011) First-principles estimates of equilibrium magnesium isotope fractionation in silicate, oxide, carbonate and hexaaquamagnesium(2+) crystals. Geochimica et Cosmochimica Acta, 75, 844–869.
Schoenberg, R., and von Blanckenburg, F. (2006) Modes of planetary-scale Fe isotope fractionation. Earth and Planetary Science Letters, 252, 342–359.
Shahar, A., Schauble, E.A., Caracas, R., Gleason, A.E., Reagan, M.M., Xiao, Y., Shu, J., and Mao, W. (2016) Pressure-dependent isotopic composition of iron alloys. Science, 352, 580–582.
Shen, G., and Heinz, D.L. (1998) High-pressure melting of deep mantle and core materials. Reviews in Mineralogy and Geochemistry, 37, 369.
Shen, G., Sturhahn, W., Alp, E.E., Zhao, J., Tollenner, T.S., Prakapenka, V.B., Meng, Y., and Mao, H.-K. (2004) Phonon density of states in iron at high pressures and high temperatures. Physics and Chemistry of Minerals, 31, 353–359.
Singwi, K.S., and Sjölander, A. (1960) Resonance absorption of nuclear gamma rays and the dynamics of atomic motions. Physical Review, 120, 1093–1102.
Sossi, P.A., Nebel, O., Anand, M., and Poitrasson, F. (2016) On the iron isotope composition of Mars and volatile depletion in the terrestrial planets. Earth and Planetary Science Letters, 449, 360–371.
Sturhahn, W. (2000) CONUSS and PHOENIX: Evaluation of nuclear resonant scattering data. Hyperfine Interactions, 125, 149–172.
——— (2001) Phase problem in synchrotron Mössbauer spectroscopy. Physical Review B, 63, 094105.
——— (2004) Nuclear resonant spectroscopy. Journal of Physics: Condensed Matter, 16, S497–S530.
——— (2020) MINeral physics UTIlity (MINUTI) open-source software package. https://www.nrixs.com/
Sturhahn, W., and Chumakov, A. (1999) Lamb–Mössbauer factor and second-order doppler shift from inelastic nuclear resonant absorption. Hyperfine Interactions, 123, 809–824.
Sturhahn, W., and Jackson, J.M. (2007) Geophysical applications of nuclear resonant scattering. In E. Ohtani, Ed., Advances in High-Pressure Mineralogy, 421, 157–174. Geological Society of America.
Toellner, T.S. (2000) Monochromatization of synchrotron radiation for nuclear resonant scattering experiments. Hyperfine Interactions, 125, 3–28.
Trueblood, K.N., Bürgi, H.B., Burzlaff, H., Dunitz, J.D., Gramaccioli, C.M., Schulz, H.H., Shmueli, U., and Abrahams, S.C. (1996) Atomic displacement parameter nomenclature. Report of a Subcommittee on Atomic Displacement Parameter Nomenclature. Acta Crystallographica, A52, 770–781.
Tse, J., Klug, D., Zhao, J., Sturhahn, W., Alp, E., Baumert, J., Gutt, C., Johnson, M., and Press, W. (2005) Anharmonic motions of Kr in the clathrate hydrate. Nature Materials, 4, 917 –921.
Urey, H.C. (1947) The thermodynamic properties of isotopic substances. Journal of the Chemical Society (Resumed), 562–581.
Vočadlo, L., and Alfe, D. (2002) Ab initio melting curve of the fcc phase of aluminum. Physical Review B, 65, 214105.
Wang, K., Moynier, F., Dauphas, N., Barrat, J.-A., Craddock, P., and Sio, C.K. (2012) Iron isotope fractionation in planetary crusts. Geochimica et Cosmochimica Acta, 89, 31–45.
Wentzcovitch, R.M., Yu, Y.G., and Wu, Z. (2010) Thermodynamic properties and phase relations in mantle minerals investigated by first principles quasiharmonic theory. Reviews in Mineralogy and Geochemistry, 71, 59–98.
Weyer, S., Anbar, A.D., Brey, G.P., Munker, C., Mezger, K., and Woodland, A.B. (2005) Iron isotope fractionation during planetary differentiation. Earth and Planetary Science Letters, 240, 251–264.
Wicks, J.K., Jackson, J.M., Sturhahn, W., and Zhang, D. (2017) Sound velocity and density of magnesiowüstites: Implications for ultralow-velocity zone topography. Geophysical Research Letters, 44, 2148–2158.
Wolf, A.S., Jackson, J.M., Dera, P., and Prakapenka, V.B. (2015) The thermal equation of state of (Mg, Fe)SiO_3 bridgmanite (perovskite) and implications for lower mantle structures. Journal of Geophysical Research: Solid Earth, 120, 7460–7489.
Wu, Z. (2010) Calculating the anharmonic free energy from first principles. Physical Review B, 81, 172301.
Yang, H., Lin, J.-F., Hu, M.Y., Roskosz, M., Bi, W., Zhao, J., Alp, E.E., Liu, J., Liu, J., Wentzcovitch, R.M., Okuchi, T., and Dauphas, N. (2019) Iron isotopic fractionation in mineral phases from Earth's lower mantle: Did terrestrial magma ocean crystallization fractionate iron isotopes? Earth and Planetary Science Letters, 506, 113–122.
Young, E.D., Galy, A., and Nagahara, H. (2002) Kinetic and equilibrium mass-dependent isotope fractionation laws in nature and their geochemical and cosmochemical significance. Geochimica et Cosmochimica Acta, 66, 1095–1104.
Yu, Y.G., Wu, Z., and Wentzcovitch, R.M. (2008) α–β–γ transformations in Mg_2SiO_4 in Earth's transition zone. Earth and Planetary Science Letters, 273, 115–122.
Yu, Y.G., Wentzcovitch, R.M., and Angel, R.J. (2010) First principles study of thermodynamics and phase transition in low-pressure ($P2_1/c$) and high-pressure ($C2/c$) clinoenstatite $MgSiO_3$. Journal of Geophysical Research, 115, B02201.
Zhang, Y., Evans, J.R.G., and Yang, S. (2011) Corrected values for boiling points and enthalpies of vaporization of elements in handbooks. Journal of Chemical & Engineering Data, 56, 328–337.
Zhang, D., Jackson, J.M., Chen, B., Sturhahn, W., Zhao, J., Yan, J., and Caracas, R. (2013) Elasticity and lattice dynamics of enstatite at high pressure. Journal of Geophysical Research: Solid Earth, 118, 4071–4082.
Zhang, D., Jackson, J.M., Zhao, J., Sturhahn, W., Alp, E.E., and Toellner, T.S., and Hu, M.Y. (2015) Fast temperature spectrometer for samples under extreme conditions. The Review of Scientific Instruments, 86, 013105.
Zhang, D., Jackson, J.M., Zhao, J., Sturhahn, W., Alp, E.E., Hu, M.Y., Toellner, T.S., Murphy, C.A., and Prakapenka, V.B. (2016) Temperature of Earth's core constrained from melting of Fe and $Fe_{0.9}Ni_{0.1}$ at high pressures. Earth and Planetary Science Letters, 447, 72–83.

Manuscript received November 9, 2020
Manuscript accepted November 2, 2021
Manuscript handled by Susannah Dorfman

Endnote:

[1]Kowalski and Jahn (2011) confused angular frequency ω with frequency ν, and thus incorrectly assigned the condition as ω (cm^{-1}) < 1.39T (K), which should be ν (cm^{-1}) < 1.39T (K), or ω (cm^{-1}) < 8.73T (K).
[2]Deposit item AM-22-37884, Online Materials. Deposit items are free to all readers and found on the MSA website, via the specific issue's Table of Contents (go to http://www.minsocam.org/MSA/AmMin/TOC/2022/Mar2022_data/Mar2022_data.html).